Charge-Sign Dependent Cosmic-Ray Modulation Observed with the Calorimetric Electron Telescope on the International Space Station
SUPPLEMENTAL MATERIAL

(CALET Collaboration)

Supplemental material relative to "Charge-Sign Dependent Cosmic-Ray Modulation Observed with the Calorimetric Electron Telescope on the International Space Station."

BACKGROUND CONTAMINATION

In each Carrington rotation period, we classify events that passed the event selection criteria (a)-(e) described in the main text into electrons and positrons (hereafter $e^{+/-}$) and protons (p) with two additional criteria (f) and (g). Criterion (f) consists of a selection performed only for $e^{+/-}$ candidates to reject protons. In criterion (f), we first collect $e^{+/-}$ candidate events using the energy deposit sum in the IMC bottom X- and Y-layers [S1]. We additionally select $e^{+/-}$ events using the energy (deposit) concentration. The latter is defined as the fraction of energy deposit in ± 9 scintillating fibers surrounding the reconstructed particle track to the total energy deposit in each layer. For each candidate $e^{+/-}$ and p events in criterion (g), we derive the distribution of the lateral spread parameter R_E defined as,

$$R_E = \sqrt{\frac{\Sigma_i \Delta E_i X_i^2}{\Sigma_i \Delta E_i}} \tag{S1}$$

where ΔE_i and X_i are the energy deposit and distance from the reconstructed track in the i-th lead tungstate crystal in the TASC top layer, respectively. The upper panel of Fig. S1 shows examples of the R_E distributions of candidate $e^{+/-}$ obtained after criteria (a)-(f) during the Carrington rotation of CR 2208 between September 2 and September 28, 2018, while the lower panel shows that of p obtained after criteria (a)-(e) without (f). It is seen that the observed distributions are well reproduced by the MC simulations. The reduced chi-square of the difference between the observed and MC R_E distributions shown in Fig. S1 are about 1.14 and 1.04 for $e^{+/-}$ and p events, respectively. We define the events with R_E below 2.0 cm in the upper panel as $e^{+/-}$ and the events with R_E above 2.0 cm in the lower panel as p. This value of $R_E = 2.0$ cm is consistent with one Molière unit in the TASC layer.

The upper panel of Fig. S2 shows the fractional contamination due to p (f_p) in the observed $e^{+/-}$ count rate ($C_{e^{+/-}\_obs}$) on the left vertical axis, while the lower panel displays the fractional contamination due to $e^{+/-}$ ($f_{e^{+/-}}$) in the observed p count rate (C_{p_obs}). We can see that f_p and $f_{e^{+/-}}$ decrease and increase with decreasing solar activity and reach minimum and maximum values when C_{e^-}, shown in Fig. 2(b) in the main text, reaches the maximum in 2020, respectively. These variations are caused by the drift effect that results in the change in the flux ratio of GCRs with $q < 0$ or $q > 0$. We calculate the fractional contamination by positrons (f_{e^+}) in $C_{e^{+/-}\_obs}$ by simply assuming that the positron flux is 7 % of the electron flux in October 2015 as reported by Aguilar *et al.* [S2] and its temporal variation in % follows the proton flux. The upper panel of Fig. S2 also shows the fractional contamination due to positrons calculated in this way on the right vertical axis. We calculate C_{e^-} and C_p using f_{e^+}, f_p, and $f_{e^{+/-}}$ in each Carrington rotation, as

$$\begin{aligned} C_{e^-} &= (1.0 - f_{e^+})(1.0 - f_p) \times C_{e^{+/-}\_obs} \ , \\ C_p &= (1.0 - f_{e^{+/-}}) \times C_{p\_obs} \ . \end{aligned} \tag{S2}$$

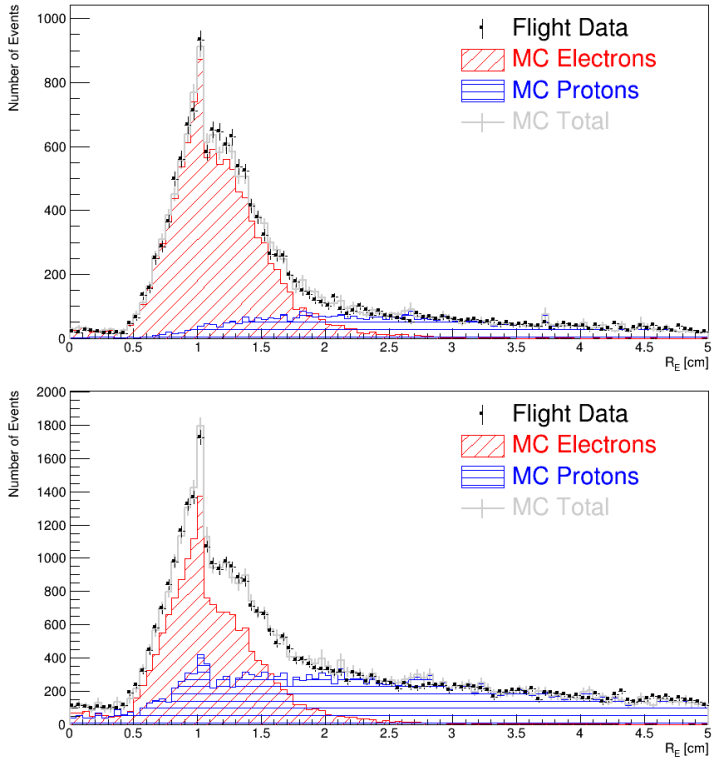

FIG. S1. R_E distribution of candidate electron (top) and proton (bottom) events during the Carrington rotation of CR 2208.

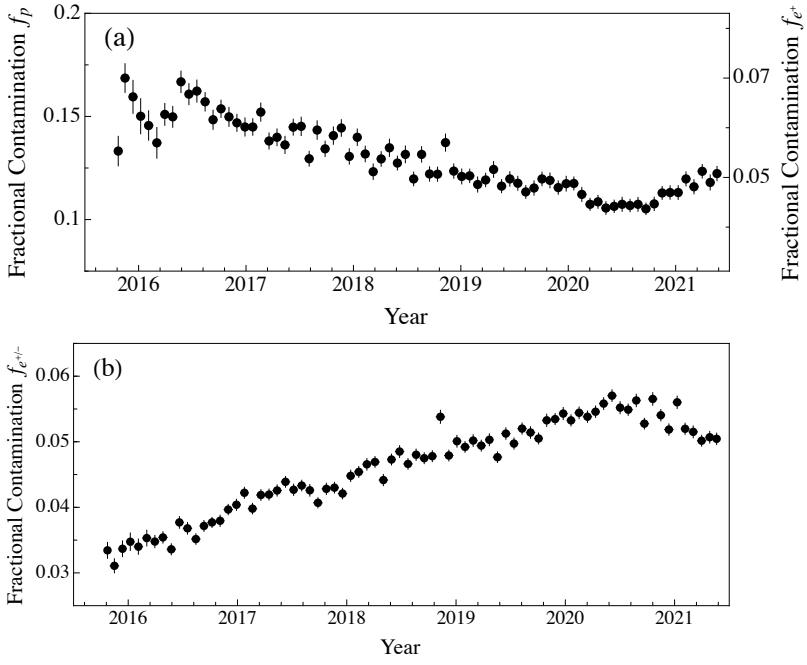

FIG. S2. (a) Temporal variations of the fractional contamination f_p by p in $C_{e^{+/-}\_obs}$ on the left vertical axis and fractional contamination f_{e^+} by e^+ in $C_{e^{+/-}\_obs}$ on the right vertical axis. (b) Electron and positron contamination $f_{e^{+/-}}$ in C_{p_obs} as a function of time.

CORRELATION BETWEEN PROTON (ELECTRON) COUNT RATES AND NEUTRON MONITOR COUNT RATES

Figure S3 shows proton (a) and electron (b) count rates at the average rigidity of 3.8 GV each as a function of the Oulu neutron monitor count rate. A good correlation in Fig. S3(a) ensures that our determination of the proton count rate is handled properly.

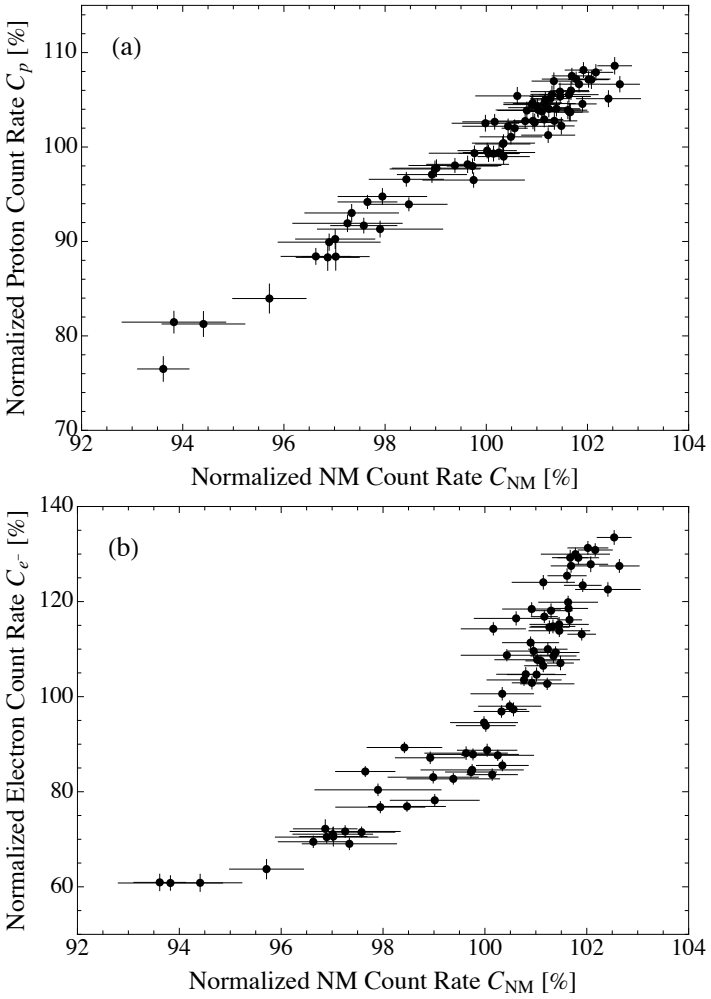

FIG. S3. CALET proton (a) and electron (b) count rates at the average rigidity of 3.8 GV as a function of neutron monitor count rates C_{NM} at the Oulu station. Correlation coefficients and regression coefficients of proton (electron) count rates with neutron monitor count rates are 0.98±0.07 (0.91±0.07) and 3.32±0.24 (9.2±0.7), respectively.

NORMALIZED COUNT RATES OF ELECTRONS AND PROTONS

Table S1 presents the normalized count rates of electrons and protons at the average rigidity of 3.8 GV, fractional contaminations due to protons and positrons in the observed $e^{+/-}$, and the fractional contamination due to $e^{+/-}$ in the observed protons, for each Carrington rotation.

TABLE S1. Electron and proton normalized count rates, C_{e^-} and C_p with statistical errors, at the average rigidity of 3.8 GV, and fractional contaminations, f_p, f_{e^+}, and $f_{e^{+/-}}$, for each Carrington rotation.

Carrington Rotation	Start Date (month/day/year)	C_{e^-} Value±Stat. (%)	C_p Value±Stat. (%)	f_p	f_{e^+}	$f_{e^{+/-}}$
CR 2169	10/13/2015	60.9±1.7	76.5±1.3	0.133±0.007	0.055±0.004	0.0334±0.0012
CR 2170	10/31/2015	60.8±1.5	81.5±1.1	0.169±0.007	0.070±0.004	0.0311±0.0011
CR 2171	11/28/2015	60.8±1.8	81.3±1.3	0.160±0.008	0.066±0.004	0.0337±0.0012
CR 2172	12/25/2015	63.7±2.0	84.0±1.5	0.150±0.009	0.062±0.004	0.0348±0.0013
CR 2173	01/21/2016	72.2±1.9	88.3±1.4	0.146±0.007	0.060±0.004	0.0340±0.0012
CR 2174	02/18/2016	70.6±2.0	88.4±1.4	0.137±0.007	0.057±0.004	0.0353±0.0012
CR 2175	03/16/2016	71.1±1.3	90.3±1.0	0.151±0.005	0.0627±0.0034	0.0348±0.0009
CR 2176	04/12/2016	69.5±1.2	88.4±0.8	0.150±0.005	0.0622±0.0033	0.0354±0.0009
CR 2177	05/09/2016	69.0±1.2	93.0±0.9	0.167±0.005	0.069±0.004	0.0336±0.0008
CR 2178	06/06/2016	71.6±1.2	91.9±0.9	0.161±0.005	0.0668±0.0035	0.0377±0.0009
CR 2179	07/03/2016	70.5±1.3	89.9±0.9	0.162±0.005	0.067±0.004	0.0368±0.0009
CR 2180	07/30/2016	71.5±1.1	91.7±0.8	0.157±0.004	0.0652±0.0033	0.0352±0.0008
CR 2181	08/27/2016	76.8±1.2	94.8±0.8	0.148±0.005	0.0616±0.0032	0.0372±0.0008
CR 2182	09/23/2016	76.9±1.0	93.9±0.7	0.154±0.004	0.0638±0.0032	0.0377±0.0008
CR 2183	10/20/2016	78.2±1.2	97.8±0.9	0.150±0.005	0.0622±0.0032	0.0380±0.0008
CR 2184	11/16/2016	82.7±1.1	98.0±0.7	0.147±0.004	0.0610±0.0030	0.0397±0.0008
CR 2185	12/14/2016	83.1±1.2	97.7±0.8	0.145±0.004	0.0602±0.0031	0.0404±0.0008
CR 2186	01/10/2017	84.1±1.1	98.0±0.8	0.145±0.004	0.0602±0.0030	0.0422±0.0008
CR 2187	02/06/2017	83.6±1.2	99.3±0.8	0.152±0.004	0.0631±0.0032	0.0398±0.0008
CR 2188	03/05/2017	85.5±1.1	99.0±0.8	0.138±0.004	0.0573±0.0029	0.0419±0.0008
CR 2189	04/02/2017	84.6±1.1	96.5±0.8	0.140±0.004	0.0581±0.0029	0.0420±0.0008
CR 2190	04/29/2017	88.7±1.3	99.3±0.9	0.136±0.004	0.0565±0.0029	0.0426±0.0008
CR 2191	05/26/2017	87.7±1.1	99.4±0.7	0.145±0.004	0.0601±0.0030	0.0439±0.0008
CR 2192	06/23/2017	88.1±1.3	98.2±0.9	0.145±0.004	0.0603±0.0031	0.0427±0.0009
CR 2193	07/20/2017	89.3±1.1	96.6±0.7	0.130±0.004	0.0538±0.0027	0.0433±0.0008
CR 2194	08/16/2017	80.4±1.2	91.3±0.8	0.143±0.004	0.0595±0.0031	0.0426±0.0009
CR 2195	09/12/2017	84.3±1.0	94.2±0.7	0.134±0.004	0.0558±0.0028	0.0407±0.0008
CR 2196	10/10/2017	87.1±1.2	97.1±0.8	0.141±0.004	0.0584±0.0030	0.0428±0.0009
CR 2197	11/06/2017	87.9±1.2	99.3±0.8	0.144±0.004	0.0600±0.0030	0.0430±0.0008
CR 2198	12/03/2017	93.9±1.2	99.6±0.8	0.131±0.004	0.0542±0.0027	0.0421±0.0008
CR 2199	12/30/2017	94.5±1.2	102.5±0.8	0.140±0.004	0.0581±0.0029	0.0448±0.0009
CR 2200	01/27/2018	96.9±1.2	100.3±0.8	0.132±0.004	0.0547±0.0027	0.0454±0.0008
CR 2201	02/23/2018	100.6±1.3	100.4±0.9	0.123±0.004	0.0512±0.0026	0.0466±0.0009
CR 2202	03/22/2018	98.0±1.1	101.1±0.7	0.1294±0.0035	0.0537±0.0026	0.0469±0.0008
CR 2203	04/19/2018	97.3±1.4	102.0±0.9	0.135±0.004	0.0560±0.0029	0.0442±0.0008
CR 2204	05/16/2018	103.5±1.1	102.7±0.8	0.1274±0.0034	0.0529±0.0026	0.0473±0.0008
CR 2205	06/12/2018	104.7±1.4	103.9±0.9	0.132±0.004	0.0546±0.0028	0.0485±0.0009
CR 2206	07/09/2018	107.5±1.2	103.8±0.8	0.1197±0.0033	0.0497±0.0025	0.0466±0.0008
CR 2207	08/06/2018	102.9±1.3	102.8±0.8	0.132±0.004	0.0546±0.0027	0.0480±0.0009
CR 2208	09/02/2018	106.5±1.2	102.9±0.8	0.1221±0.0035	0.0507±0.0025	0.0475±0.0008
CR 2209	09/29/2018	102.7±1.2	101.3±0.8	0.1220±0.0034	0.0507±0.0025	0.0478±0.0008
CR 2210	10/26/2018	104.6±1.4	104.2±0.9	0.137±0.004	0.0570±0.0029	0.0538±0.0010
CR 2211	11/23/2018	107.8±1.2	103.9±0.8	0.1235±0.0035	0.0513±0.0026	0.0479±0.0008
CR 2212	12/20/2018	109.6±1.4	102.6±0.9	0.121±0.004	0.0502±0.0026	0.0501±0.0009
CR 2213	01/16/2019	111.4±1.2	104.5±0.7	0.1212±0.0032	0.0503±0.0025	0.0492±0.0008
CR 2214	02/13/2019	108.6±1.4	102.8±0.9	0.117±0.004	0.0486±0.0025	0.0502±0.0009
CR 2215	03/12/2019	109.3±1.2	104.1±0.8	0.1192±0.0033	0.0495±0.0024	0.0494±0.0008
CR 2216	04/08/2019	107.1±1.4	102.2±0.9	0.124±0.004	0.0516±0.0027	0.0503±0.0009
CR 2217	05/05/2019	108.7±1.2	102.2±0.8	0.1162±0.0032	0.0482±0.0024	0.0477±0.0008

Continued on next page

TABLE S1. — *Continued from previous page*

Carrington Rotation	Start Date (month/day/year)	C_{e^-} Value±Stat. (%)	C_p Value±Stat. (%)	f_p	f_{e^+}	$f_{e^{+/-}}$
CR 2218	06/02/2019	110.0±1.3	104.0±0.8	0.1197±0.0035	0.0497±0.0025	0.0513±0.0009
CR 2219	06/29/2019	114.6±1.3	105.1±0.8	0.1176±0.0034	0.0488±0.0025	0.0497±0.0008
CR 2220	07/26/2019	116.8±1.2	105.0±0.8	0.1134±0.0031	0.0471±0.0023	0.0520±0.0008
CR 2221	08/23/2019	118.1±1.4	105.6±0.9	0.1153±0.0035	0.0479±0.0024	0.0514±0.0009
CR 2222	09/19/2019	113.1±1.2	104.6±0.8	0.1197±0.0033	0.0497±0.0025	0.0505±0.0008
CR 2223	10/16/2019	116.2±1.4	103.7±0.9	0.119±0.004	0.0494±0.0025	0.0533±0.0009
CR 2224	11/12/2019	119.9±1.3	105.5±0.8	0.1155±0.0032	0.0480±0.0024	0.0535±0.0008
CR 2225	12/10/2019	118.6±1.5	103.7±0.9	0.117±0.004	0.0487±0.0025	0.0543±0.0009
CR 2226	01/06/2020	123.4±1.3	108.2±0.8	0.1175±0.0031	0.0488±0.0024	0.0533±0.0008
CR 2227	02/02/2020	122.5±1.4	105.1±0.8	0.1122±0.0034	0.0466±0.0024	0.0544±0.0009
CR 2228	02/29/2020	130.9±1.3	107.9±0.8	0.1074±0.0029	0.0446±0.0022	0.0538±0.0009
CR 2229	03/28/2020	127.5±1.4	106.7±0.8	0.1086±0.0031	0.0451±0.0023	0.0546±0.0009
CR 2230	04/24/2020	133.5±1.4	108.6±0.9	0.1056±0.0031	0.0438±0.0022	0.0558±0.0009
CR 2231	05/21/2020	131.3±1.3	107.2±0.8	0.1064±0.0030	0.0442±0.0022	0.0570±0.0009
CR 2232	06/18/2020	127.9±1.6	107.1±0.9	0.1074±0.0034	0.0446±0.0023	0.0552±0.0009
CR 2233	07/15/2020	129.2±1.3	106.7±0.8	0.1068±0.0030	0.0443±0.0022	0.0549±0.0009
CR 2234	08/11/2020	129.2±1.5	106.0±0.9	0.1074±0.0034	0.0446±0.0023	0.0563±0.0010
CR 2235	09/07/2020	130.0±1.2	107.2±0.7	0.1052±0.0028	0.0437±0.0021	0.0528±0.0008
CR 2236	10/05/2020	125.4±1.4	103.9±0.9	0.1076±0.0033	0.0447±0.0023	0.0565±0.0010
CR 2237	11/01/2020	127.5±1.3	107.5±0.8	0.1129±0.0031	0.0469±0.0023	0.0540±0.0009
CR 2238	11/28/2020	118.4±1.3	104.7±0.8	0.1131±0.0032	0.0470±0.0024	0.0519±0.0009
CR 2239	12/25/2020	124.1±1.4	104.6±0.9	0.1131±0.0033	0.0470±0.0024	0.0560±0.0009
CR 2240	01/22/2021	114.3±1.3	102.7±0.8	0.1197±0.0034	0.0497±0.0025	0.0520±0.0008
CR 2241	02/18/2021	116.5±1.4	105.4±0.9	0.1159±0.0034	0.0481±0.0024	0.0515±0.0009
CR 2242	03/17/2021	113.9±1.2	105.3±0.8	0.1234±0.0033	0.0512±0.0025	0.0502±0.0008
CR 2243	04/14/2021	115.2±1.4	105.9±0.9	0.118±0.004	0.0490±0.0025	0.0507±0.0009
CR 2244	05/11/2021	114.8±1.3	107.0±0.9	0.1223±0.0035	0.0508±0.0025	0.0505±0.0009

NUMERICAL DRIFT MODEL OF THE SOLAR MODULATION

The transport of GCRs in the heliosphere is described by the Fokker-Planck equation,

$$\frac{\partial f}{\partial t} = \boldsymbol{\nabla} \cdot (\boldsymbol{\kappa} \cdot \boldsymbol{\nabla} f - \boldsymbol{V}_{\rm SW} f) + \frac{1}{3p^2}(\boldsymbol{\nabla} \cdot \boldsymbol{V}_{\rm SW}) \frac{\partial}{\partial p}(p^3 f), \tag{S3}$$

where $f(\boldsymbol{r}, p, t)$ is the phase space distribution function of GCRs with momentum p at position $\boldsymbol{r}$ and time t, $\boldsymbol{V}_{\rm SW}$ is the solar wind speed and $\boldsymbol{\kappa}$ is the spatial diffusion tensor. We obtain the solution f at Earth by calculating the following set of the stochastic differential equations (SDEs) which are mathematically equivalent to Eq. (S3) [S3–S7],

$$\begin{aligned} d\boldsymbol{r} &= (\boldsymbol{\nabla} \cdot \boldsymbol{\kappa} + \boldsymbol{V}_{\rm SW} + \boldsymbol{V}_{\rm D})dt + \textstyle\sum_s \boldsymbol{\sigma}_s dW_s(t) \ , \\ dp &= -\frac{1}{3} p (\boldsymbol{\nabla} \cdot \boldsymbol{V}_{\rm SW}) dt \ , \end{aligned} \tag{S4}$$

where $\boldsymbol{V}_{\rm D}$ is the gradient-curvature drift velocity, $\boldsymbol{\sigma}_s$ is the tensor which gives $\sum_s \sigma_s^\mu \sigma_s^\nu = 2\kappa^{\mu\nu}$ with $\kappa^{\mu\nu}$ denoting the $\mu\nu$ element of $\boldsymbol{\kappa}$, dW_s is a vector denoting the random-walk along the s-axis according to the Gaussian probability distribution of the Wiener process [S8].

The diffusion tensor $\boldsymbol{\kappa}$ in a coordinate system in which the x-axis points away from the Sun along the magnetic field line, the y-axis is directed southward perpendicular to a plane including the magnetic field line and the radial vector, and the z-axis completes the right-handed coordinated system, is written as

$$\boldsymbol{\kappa} = \begin{pmatrix} \kappa_\parallel & 0 & 0 \\ 0 & \kappa_{\perp 1} & 0 \\ 0 & 0 & \kappa_{\perp 2} \end{pmatrix} \ . \tag{S5}$$

We define the diffusion coefficients in terms of the particle's velocity (v) and momentum (p) and the strength of the heliospheric magnetic field (HMF) (B) at the particle's location, as

$$\begin{aligned} \kappa_\parallel &= \kappa_\parallel^0 \beta \left(\frac{p}{1{\rm GeV/c}} \right)^a \left(\frac{B_{\rm E}}{B} \right)^{b_\parallel} \ , \\ \kappa_{\perp 1} &= \kappa_{\perp 1}^0 \beta \left(\frac{p}{1{\rm GeV/c}} \right)^a \left(\frac{B_{\rm E}}{B} \right)^{b_{\perp 1}} \ , \\ \kappa_{\perp 2} &= \kappa_{\perp 2}^0 \beta \left(\frac{p}{1{\rm GeV/c}} \right)^a \left(\frac{B_{\rm E}}{B} \right)^{b_{\perp 2}} \ , \end{aligned} \tag{S6}$$

where β is the particle's velocity relative to the speed of light (c) and $B_{\rm E}$ is B at Earth. $\kappa_\parallel^0$, $\kappa_{\perp 1}^0$, $\kappa_{\perp 2}^0$, a, $b_\parallel$, $b_{\perp 1}$, and $b_{\perp 2}$ are free parameters which are set to $\kappa_\parallel^0 = 1 \times 10^{22}$ cm^2/s, $\kappa_{\perp 1}^0 = 2 \times 10^{20}$ cm^2/s, $\kappa_{\perp 2}^0 = 1 \times 10^{20}$ cm^2/s, $a = 1.0$, $b_\parallel = 1.0$, $b_{\perp 1} = 1.4{\rm cos}^2\theta + 0.6{\rm sin}^2\theta$, and $b_{\perp 2} = 1.0$, respectively, where θ is the colatitude of the particle's location in the heliocentric polar coordinate system, for the best reproduction of the GCR energy spectra observed at Earth [S9].

The $\boldsymbol{V}_{\rm D}$ of a particle in the HMF $\boldsymbol{B}$ is given as [S10]

$$\boldsymbol{V}_{\rm D} = \frac{pvc}{3qB^4} \left[B^2 (\boldsymbol{\nabla} \times \boldsymbol{B}) + \boldsymbol{B} \times \boldsymbol{\nabla} B^2 \right], \tag{S7}$$

where q is the particle's charge. To calculate $\boldsymbol{V}_{\rm D}$ in Eq. (S7) at the particle's location, we adopt the Parker-Spiral HMF in the heliocentric polar coordinate system formed with unit vectors ($\boldsymbol{e}_r$, $\boldsymbol{e}_\theta$, $\boldsymbol{e}_\phi$) defined as

$$\boldsymbol{B} = B_{\rm E} (\frac{r_{\rm E}}{r})^2 \left(\boldsymbol{e}_r - \frac{r \Omega_\odot \sin\theta}{V_{\rm SW}} \boldsymbol{e}_\phi \right) \left[1 - 2H(\theta - \theta') \right], \tag{S8}$$

where r is the radial distance from the Sun, $B_{\rm E}$ is the strength of $\boldsymbol{B}$ observed at Earth where $r = r_{\rm E}$ and $\theta = 90°$, $\Omega_\odot$ is the angular velocity of the solar rotation and H is the Heaviside step function denoting the abrupt reversal of the $\boldsymbol{B}$ orientation across the Heliospheric Current Sheet (HCS) at $\theta = \theta'$. In the present model, $\boldsymbol{V}_{\rm SW}$ is assumed to

be radial and constant during each solar rotation period (with its magnitude calculated from the rotation average of $V_{\rm SW}$ observed at Earth). We model the HCS location (θ') at r, ϕ and t, as

$$\theta' = \frac{\pi}{2} - \sin^{-1}\left[\sin\alpha \sin\left(\phi - \phi_E - \Omega_\odot t + \frac{(r - r_\odot)\Omega_\odot}{V_{\rm SW}}\right)\right], \tag{S9}$$

where ϕ is the heliospheric azimuth angle, ϕ_E is ϕ of Earth, $r_\odot$ is the radius of the Sun, and α is the HCS tilt angle which is assumed to be constant during each solar rotation period. Taking account of the solar wind propagation to the particle's location, we calculate $\boldsymbol{B}$ at $\boldsymbol{r}$ and t from $B_{\rm E}$ observed at Earth at $t - r/V_{\rm SW}$ by Eq. (S9). It is noted that Eq. (S7) cannot be used to calculate the $\boldsymbol{V}_{\rm D}$ of particles crossing the HCS where $\boldsymbol{B}$ reverses discontinuously. The modeling of the drift velocity of particles meandering along the HCS is very crucial, because it is expected to be much faster than the solar wind and the typical amount of diffusion [S11, S12]. By including a modification to the model by Burger and Potgieter [S12] that makes it insensitive to the structure of the HCS as the particle's Larmor radius ($R_{\rm L}$) increases, we calculate the magnitude of the drift velocity along the HCS ($V_{\rm HCS}$), as

$$V_{\rm HCS} = \left[0.457 - 0.412\left(\frac{d}{\lambda_{\rm HCS} R_{\rm L}}\right) + 0.0915\left(\frac{d}{\lambda_{\rm HCS} R_{\rm L}}\right)^2\right] \lambda_{\rm HCS} v \ , \tag{S10}$$

with

$$\lambda_{\rm HCS} = \begin{cases} 1 & , \quad \text{if } R_{\rm L} \le V_{\rm SW} T_{\rm S} \\ \dfrac{V_{\rm SW} T_{\rm S}}{R_{\rm L}} & , \quad \text{if } R_{\rm L} > V_{\rm SW} T_{\rm S} \end{cases} , \tag{S11}$$

where d is the minimum distance between the particle and the HCS, and $T_{\rm S}$ is the rotation period of the Sun. The above $V_{\rm HCS}$ is applied only for particles near the HCS within $d/R_{\rm L} < 2\lambda_{\rm HCS}$.

The second equation of Eq. (S4) denotes the adiabatic cooling of GCRs in an expanding solar wind. By reversing the sign of the velocity ($\boldsymbol{V}_{\rm SW}$ and $\boldsymbol{V}_{\rm D}$), we solve Eq. (S4) backward in time and trace the particle's trajectory in phase space from Earth at $\boldsymbol{r}_{\rm E}$ until the particle arrives back at the outer boundary at $\boldsymbol{r}_{\rm out}$, which is assumed to be a sphere centered at the Sun with a radius of 100 AU. By repeating this calculation for a sufficient number of particles, we obtain a distribution function $F(\boldsymbol{r}_{\rm E}, p_{\rm E} | \boldsymbol{r}_{\rm out}, p)$ which gives the probability of a particle with $p_{\rm E}$ at Earth to reach the outer boundary with p. We then calculate the phase space distribution of GCRs $f_{\rm E}(p_{\rm E})$ at Earth, as

$$f_E(p_{\rm E}) = \int f_{\rm LIS}(p) F(p_{\rm E}, \boldsymbol{r}_{\rm E} \mid p, \boldsymbol{r}_{\rm out}) dp \ , \tag{S12}$$

where $f_{\rm LIS}(p)$ is the phase space distribution of GCRs in local interstellar space. We calculate $f_{\rm LIS}(p)$ by using the following empirical LIS spectra of GCRs, $J_p(E) = f_{{\rm LIS}_p}(p)p^2$ for GCR protons and $J_{e^-}(E) = f_{{\rm LIS}_{e^-}}(p)p^2$ for GCR electrons. We adopt $J_p(E)$ as a function of the kinetic energy E,

$$J_p(E) = 16.0\left(1 + \frac{4.2}{E^{1.22}} + \frac{1.3}{E^{2.8}} + \frac{0.0087}{E^{4.32}}\right)^{-1} E^{-2.73} \ . \tag{S13}$$

We also adopt the $J_{e^-}(E)$ proposed by Potgieter [S13] with an additional modulation of $\phi = 350$ MV based on the force-field approximation [S14]. The additional force-field modulation is due to the modelling of solar modulation in the heliosheath.

[S1] Y. Asaoka, Y. Ozawa, S. Torii, *et al.* (CALET Collaboration), Astropart. Phys. **100**, 29 (2018).
[S2] M. Aguilar, L. A. Cavasonza, G. Ambrosi, L. Arruda, N. Attig, *et al.* (AMS Collaboration), Physical Review Letters **121**, 051102 (2018).
[S3] Y. Yamada, S. Yanagita, and T. Yoshida, Geophys. Res. Lett. **25**, 2353 (1998).
[S4] M. Zhang, Astrophysical Journal **513**, 409 (1999).
[S5] C. Pei, J. W. Bieber, R. A. Burger, and J. Clem, Journal of Geophysical Research **115**, A12107 (2010).
[S6] R. D. Strauss, M. S. Potgieter, I. B'usching, and A. Kopp, Astrophys. Space Sci. **339**, 223 (2012).
[S7] S. Miyake, R. Kataoka, and T. Sato, Spece Weather **15**, 589 (2017).

[S8] C. W. Gardiner, *Handbook of Stochastic Differential Equations* (Princeton Univ. Press, Princeton, 1989).
[S9] S. Miyake, in *Proceedings of Science (ICRC2017)*, 018 (2017).
[S10] P. A. Isenberg and J. R. Jokipii, Astrophys. J. **234**, 746 (1979).
[S11] J. Kóta and J. R. Jokipii, Aptrophys. J. **265**, 573 (1983).
[S12] R. A. Burger and M. S. Potgieter, Astrophys. J. **339**, 501 (1989).
[S13] M. S. Potgieter, E. E. Vos, R. Munini, M. Boezio, and V. D. Felice, Astrophysical Journal **810**, 141 (2015).
[S14] L. J. Gleeson and W. I. Axford, Astrophys. J. **154**, 1011 (1968).